RSC Advances

ROYAL SOCIETY OF CHEMISTRY

www.rsc.org/advances

Journal Name RSCPublishing

ARTICLE

Fabrication of black hierarchical TiO_2 nanostructures with enhanced photocatalytic activity

Cite this: DOI: 10.1039/x0xx00000x

Received 00th January 2012,
Accepted 00th January 2012

DOI: 10.1039/x0xx00000x

www.rsc.org/

Bo Chen, [a,*] Jeremy A. Beach,[b] Deepam Maurya, [a] Robert B. Moore [b] and Shashank Priya [a,*]

Here, we report the fabrication of hierarchical TiO_2 nanostructures with wire-in-tube architectures by hydrothermal treatment of anodic TiO_2 nanotubes. The mechanism for this morphological evolution was understood by dissolution-precipitation of TiO_6^{2-} octahedra. Sintering the hierarchical TiO_2 nanostructures under vacuum condition created black TiO_2 nanostructures, which shown anatase phase with self-doped Ti^{3+} present in the bulk. Due to reduced band gap, increased donor density, and enlarged active interface, the black hierarchical TiO_2 nanostructures demonstrated efficient photocatalytic performance under both full spectrum and visible light illumination.

Introduction

Due to its favorable band-edge positions, high chemical stability, excellent photocorrosion resistance, nontoxicity, and low cost, TiO_2 has attracted broad interest as one of the most promising photocatalysts for use in solar water splitting and degradation of organic pollutants.[1, 2] Up to now, various TiO_2 structures (such as nanotubes, nanoparticles, nanorods, nanowires, flower-like clusters, microspheres) have been synthesized.[3-18] Among them, anodic TiO_2 nanotube arrays prepared by electrochemical anodization distinguish themselves due to the facile synthesis procedure and controllable resultant morphologies (such as diameter, length, and density of nanotubes).[7-10] Moreover, anodic TiO_2 nanotubes provide one-dimensional electron transport pathways for efficient charge transfer, which reduces the recombination of photo-excited electron-hole pairs and increases the photocatalytic performance. However, the anodic TiO_2 nanotube arrays exhibit a low surface area which leads to inefficient active interface with the electrolyte for charge transfer to occur.[11, 12] Therefore, fabrication of novel one-dimensional TiO_2 nanostructures with a high surface area is essential for further increasing the photocatalytic performance.

Wide bandgap of TiO_2 (3.2 eV for anatase and brookite, 3.0 eV for rutile) significantly limits its photocatalytic application, because it can only be activated by ~5% of the available sunlight energy.[19-22] Therefore, enormous efforts have focused on narrowing the bandgap to enhance the photocatalytic performance of TiO_2. Recently, reduced black TiO_2 has emerged as an effective strategy towards small bandgap TiO_2.[13-18] Chen et al. synthesized reduced black TiO_2 nanoparticles with surface disorder and a bandgap of ~1.0 eV in a high-pressure H_2 atmosphere, which exhibited visible light absorption and high H_2 production capability.[13] Li et al. reported the improved water splitting performance of rutile TiO_2 nanowires after annealing in a H_2 atmosphere, which was ascribed to the formation of oxygen vacancy sites.[14] Zheng et al. found that the surface Ti-H bonds on hydrogenated TiO_2 nanowire-microspheres increases both the visible light absorption and photocatalytic activity.[15] Naldoni et al. fabricated the black TiO_2 nanoparticles with self-doped Ti^{3+}, which exhibited a narrow bandgap (1.85 eV), by freezing the surface disorder during H_2 treatment to form a crystalline core/disorder shell structure.[16] Even though the reduced TiO_2 obtained from H_2 treatment exhibited improved photocatalytic activities, the reason was related to increased efficiency in UV light region and not to the enhanced visible light absorption.[13-15] However, it is more important to extend the working spectrum of TiO_2 photocatalysis into visible light region, which contributes 43% of the solar energy. It is not clear if annealing the TiO_2 nanostructures in the vacuum conditions could generate black TiO_2 nanostructures which have visible-light-induced photocatalytic activities.

In this study, novel hierarchical TiO_2 nanostructures with wire-in-tube architectures were fabricated by hydrothermal treatment of anodic TiO_2 nanotube arrays. Furthermore, the hydrothermally treated samples were modified into reduced black TiO_2 by annealing under vacuum at 450°C for 2 hours. The structural and electronic properties of the resulting black hierarchical TiO_2 nanostructures were thoroughly studied. The intended effect of the hydrothermal treatment and vacuum sintering was to enhance the surface area available for photocatalytic activities and to expand the absorption spectrum of the TiO_2, respectively.

Experimental

Anodic TiO_2 nanotube arrays were fabricated by a two-step anodization approach described in detail elsewhere.[23, 24] Briefly, the first layer of nanotubular TiO_2 was synthesized by anodizing Ti foil at 60 V for 90 min in ethylene glycol electrolyte containing 0.3 wt% NH_4F and 2 vol% DI water. The first nanotubular layer was subsequently removed by ultrasonication in DI water for 10 min. Finally, as-anodized TiO_2 nanotube arrays were grown by a second-step anodization under the same conditions as the first layer for 30 min. After anodization, hierarchical TiO_2 nanostructures (H-TiO_2) were produced by hydrothermal treatment in a 45 mL Teflon-lined autoclave containing 13.5 mL solution (DI water, HCl with PH=3, or NH_4OH with pH=11) at 120 ºC for 20-60 min. In the second processing step, the hydrothermally-treated samples (H-TiO_2) were sealed in a quartz tube under vacuum condition (10^{-6} Torr) and annealed at 450 ºC for 2 h with a heating and cooling rate of 2 ºC/min, described here as "vacuum-H-TiO_2". Some hydrothermally-treated TiO_2 nanostructures were also annealed in air at 450 ºC for 2 h, referred to as "air-H-TiO_2". For comparative analysis, some as-anodized TiO_2 nanotubes were annealed in air at 450 ºC for 2 h, described in this study as "air-TiO_2".

The morphology and crystalline structure of as-anodized, hydrothermally treated, and vacuum annealed TiO_2 nanostructures was characterized by scanning electron microscopy (SEM, Quanta 600 FEG, FEI Company) and X-ray diffraction (XRD, X'Pert PRO, PANalytical Inc.). TEM analysis was performed using a FEI Titan 80–300 transmission electron microscope. The photocatalytic activities were evaluated by 10^{-5} M methylene blue degradation. The full spectrum light source was AM 1.5 (100 mW/cm^2) illumination with a solar simulator (150 W Sol 2A^{TM}, Oriel) and visible light illumination was created by applying an ultraviolet cut-on filter (cut-on wavelength at 400 nm) to the solar simulator. UV-visible absorbance was measured by a UV-Vis-NIR spectrophotometer (Hitachi U-4100). Raman spectra were acquired using a Raman spectrometer (Senterra, Bruker Corporation) with a laser excitation of 532 nm. Electron paramagnetic resonance (EPR) spectra were collected at room temperature by a Bruker ER 200D-SRC electron spin resonance. X-ray photoelectron spectroscopy (XPS) spectra were recorded by a scanning photoelectron spectrometer microprobe (PHI Quantera SXM) using Al Kα radiation at a power of 50 W with pass energy of 26 eV. The binding energy was calibrated by referencing the C 1s peak at 284.6 eV. Mott-Schottky plots were obtained by electrochemical impedance spectroscopy (EIS) analysis in 1 M KOH in a darkroom under different bias potentials (E) with an excitation voltage of 10 mV and an applied frequency (f) ranging from 0.1 Hz to 100 kHz.

Results and discussion

A morphological transformation occurred in the anodic TiO_2 nanotubes when they were hydrothermally treated in DI water for increasing periods of time. As-anodized TiO_2 nanotubes had a smooth tube surface (Fig. 1a). After 25 min of hydrothermal treatment in DI water, many nanoparticles developed at the inner surface of the TiO_2 nanotubes (Fig. 1b). Interestingly, when the hydrothermal treatment was increased to 30 min, a nanowire with numerous nanoparticles covering its surface grew inside each nanotube as a wire-in-tube architecture (Fig. 1c). In the meantime, the outer shell of nanotubes shrank to 20 nm. Prolonging the hydrothermal treatment to 40 min caused further shrinkage of the outer shell while the diameter of inner wire continued to increase to the point where it became difficult to distinguish the tube from the wire (Fig. 1d).

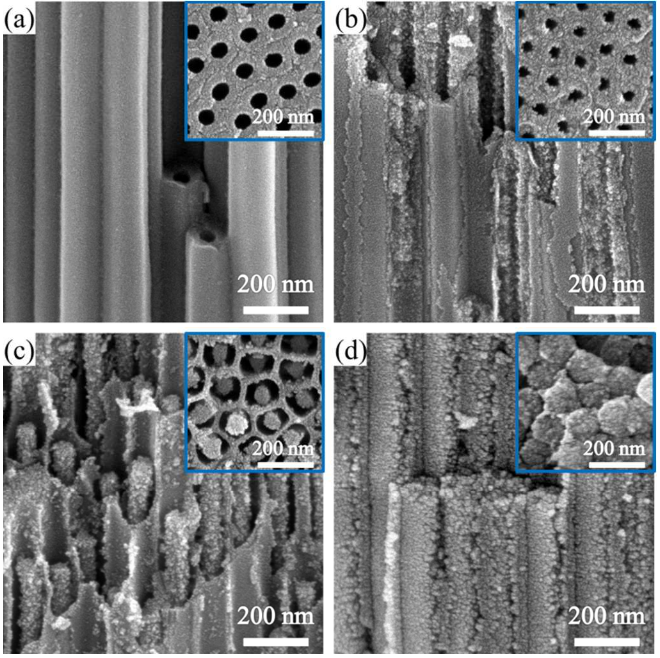

Fig 1. SEM image of anodic TiO_2 nanotubes after hydrothermal treatment in DI water at 120 ºC with different times: (a) 0 min; (b) 25min, (c) 30 min, (d) 40 min. The inset is cross-section image.

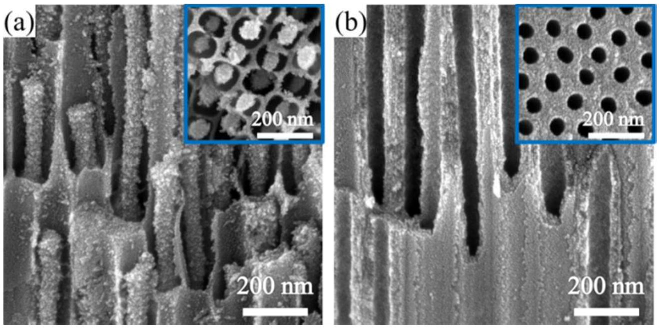

Fig. 2. SEM image of the anodic TiO_2 nanotubes after hydrothermal treatment in (a) HCl with pH=3 at 120 ºC for 20 min, (b) NH_4OH with pH=11 for 60 min. The inset is cross-section image.

The pH value of solution during hydrothermal treatment of TiO_2 nanotubes crucially influenced the morphological transformation. When the DI water in solution was replaced with aqueous HCl with PH=3, the rate of the morphological transformation was accelerated and similar wire-in-tube architectures were achieved within 20 min (Fig. 2a). On the other hand, hydrothermal treatment in alkaline solution retarded the development of wire-in-tube architectures. As shown in Fig. 2b, even after 60 min of hydrothermal treatment in NH_4OH with pH=11, TiO_2 maintained the nanotubular structure without development of any nanoparticles or nanowires inside nanotubes.

In order to understand the mechanism of morphological transformation during hydrothermal treatment, the phase evolution was also investigated by XRD analysis (Fig. 3). As-grown anodic TiO_2 nanotubes were amorphous. With the development of wire-in-tube architecture when hydrothermally treated in DI water or HCl solution (as shown in Fig. 1 and Fig. 2), diffraction peaks appeared at 25.4°, 37.9°, 48.2°, 55°, and 62.9°. These peaks were attributed to the diffraction of anatase TiO_2, indicating that the amorphous as-grown TiO_2 transformed into anatase TiO_2. Alkaline solution not only hindered morphological transformation but also hindered the formation of anatase phase. After 60 min hydrothermal treatment in NH_4OH solution, no obvious anatase TiO_2 XRD peak was observed.

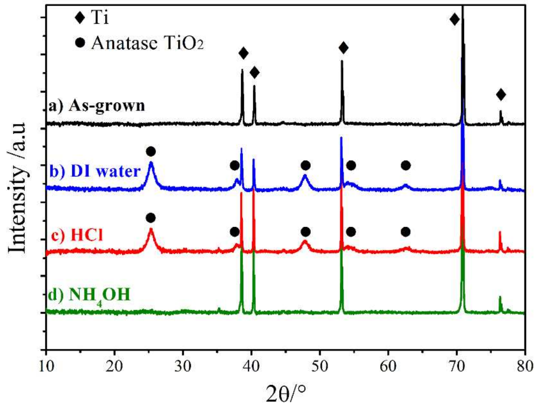

Fig. 3. XRD patterns of TiO_2 nanostructures after different hydrothermal treatment conditions: (a) as-grown TiO_2 nanotubes, (b) DI water for 30 min, (c) HCl with pH=3 for 20 min, and (d) NH_4OH with pH=11 for 60 min.

The dissolution-precipitation of TiO_6^{2-} octahedra during hydrothermal treatment prompted the transformation of amorphous TiO_2 into anatase (Fig. 4a). It is well known that multiple TiO_2 polymorphs (amorphous, anatase, rutile, and brookite) are all composed of TiO_6^{2-} octahedra, however, they differ in their shared corners and edges. Under the hydrothermal condition in DI water, the surface of amorphous TiO_2 underwent a dissolution process to create hydrated octahedral complexes of $[Ti(O)_m(OH)_n(OH_2)_{6-m-n}]^{(2m+n-4)-}$ with Ti-OH and Ti-OH_2^+ surface groups. Ti-OH and Ti-OH_2^+ groups on the adjacent hydrated octahedra experienced olation-oxolation processes to construct Ti-O-Ti bridges by eliminating a water molecule. Since the anatase phase shows lower Gibbs free energy than rutile phase, the olation-oxolation process rearranged the TiO_6^{2-} octahedra in zigzag chains and precipitated anatase TiO_2. In acidic solution, the H^+ ions promoted more Ti-OH and Ti-OH_2^+ surface groups, and thus expedited the olation-oxolation process. However, in alkaline solution, the OH^- ions suppressed the formation of protonated Ti-OH_2^+ on the TiO_2 surface, which significantly retarded the dissolution-precipitation of TiO_6^{2-} octahedra, thus no anatase phase was formed.

The morphological evolution can also be understood by the dissolution-precipitation process (Fig. 4b). During hydrothermal treatment, the hydrated octahedral complexes developed near inner surface of nanotubes. The olation-oxolation process aggregated those hydrated octahedra and precipitated anatase TiO_2 at inner surface of nanotubes. It is reported that the anodic TiO_2 nanotubes have double shell structures with an outer shell denser than the inner shell.[25] Therefore, the dissolution-precipitation process at the outer shell was slow, while the inner shell preferentially dissolved and precipitated an anatase TiO_2 nanowire inside the outer shell to generate wire-in-tube architecture. The outer shell also dissolved and shrank with increasing hydrothermal treatment time. Eventually, the interior TiO_2 nanowires would fully fill the nanotubes.

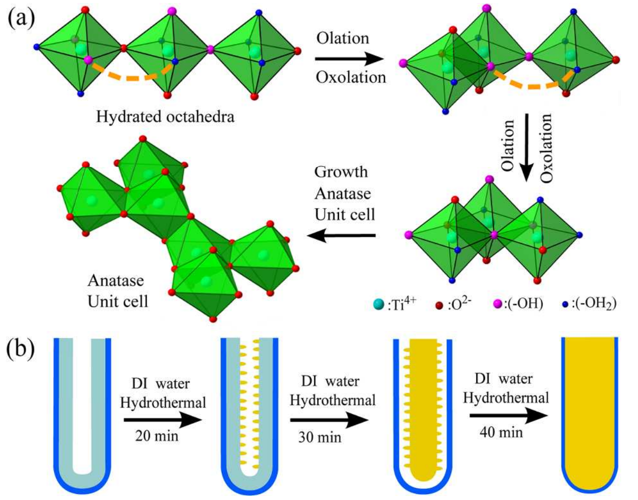

Fig. 4. Schematic illustration of (a) phase evolution and (b) morphological transformation during hydrothermal treatment of anodic TiO_2 nanotubes.

Next, the effect of sintering atmosphere on TiO_2 nanostructures was investigated. Fig. 5 shows the morphologies of as-synthesized wire-in-tube TiO_2 architecture (Fig. 1c) after sintering in air and vacuum condition, respectively. Compared with the as-synthesized wire-in-tube architecture, the air-sintered hierarchical TiO_2 (air-H-TiO_2) sample exhibited no obvious morphological changes (Fig. 5a). The vacuum-sintered (vacuum-H-TiO_2) sample maintained the wire-in-tube architecture (Fig. 5b); however, sintering in vacuum condition led to the growth of nanoparticles decorated on the surface of inner-nanowires and the development of nanoparticles on the tubular outer-shell. Moreover, the vacuum-H-TiO_2 sample exhibited a black color. Sintering under the vacuum condition leads to the vapor transport plays a dominating role during the sintering, while reducing the driving force for densification due to the coarsening effect.[26] As a result, the coarsening by the vapor transport mechanism increases the nanoparticles grain size for the vacuum-H-TiO_2 samples.

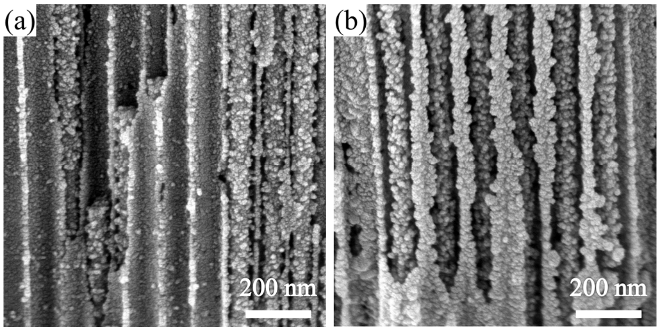

Fig. 5. SEM images of as-synthesized wire-in-tube TiO_2 architecture after sintering in (a) air and (b) vacuum condition.

TEM images provided detail information on the structure of vacuum-H-TiO_2 samples. TEM sample preparation was carried out by ultrasonic vacuum-H-TiO_2 nanostructures in ethanol. As shown in Fig. 6, both the nanowires and nanotubes were composed by TiO_2 nanoparticles with diameter around 10 nm. Fig. 6c and 6d demonstrated clear lattice fringes with inter-planar spacing of 0.35 nm, corresponding to (101) planes of anatase TiO_2. Similarly to the black TiO_2 created by hydrogen treatment, the nanoparticles in the vacuum-H-TiO_2 samples have a shallow disordered surface layer around 0.5 nm.[13,16]

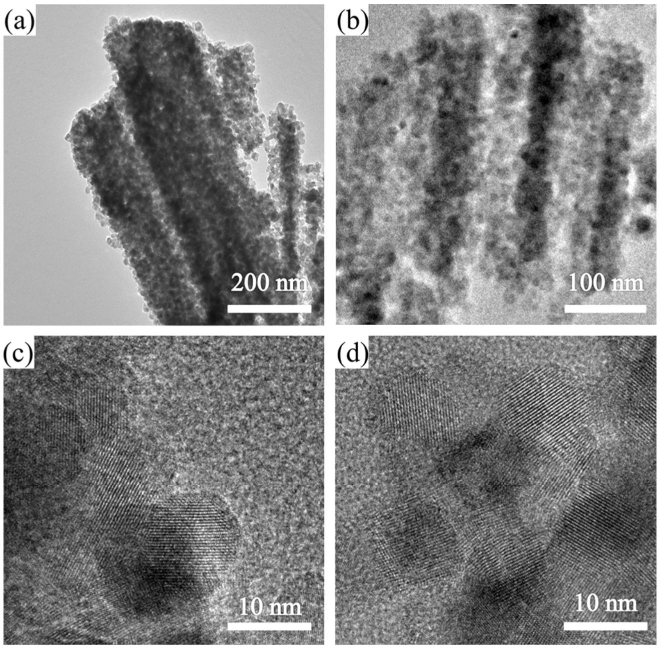

Fig. 6. TEM images of vacuum-H-TiO_2 samples.

The structural properties of black TiO_2 were identified by XRD and Raman spectrum. Excluding the XRD peaks from the Ti metallic substrate, air-TiO_2, air-H-TiO_2 and vacuum-H-TiO_2 samples demonstrated similar crystalline structure with anatase phase present in all samples (Fig. 7a). Raman spectra of all samples displayed typical anatase Raman bands with three E_g, one B_{1g}, and one A_{1g} active modes (Fig. 7b). However, the peak position of the most intense anatase E_g mode at 143.8 cm^{-1} was red-shifted to 150.4 cm^{-1} for black TiO_2. This red-shift of the E_g Raman mode can be attributed to the reduced TiO_{2-x} with increase in Ti^{3+}, which is similar to previous reports.[27, 28] In addition, all Raman-active modes of vacuum-H-TiO_2 were broadened compared with those of air-TiO_2 and air-H-TiO_2 samples.

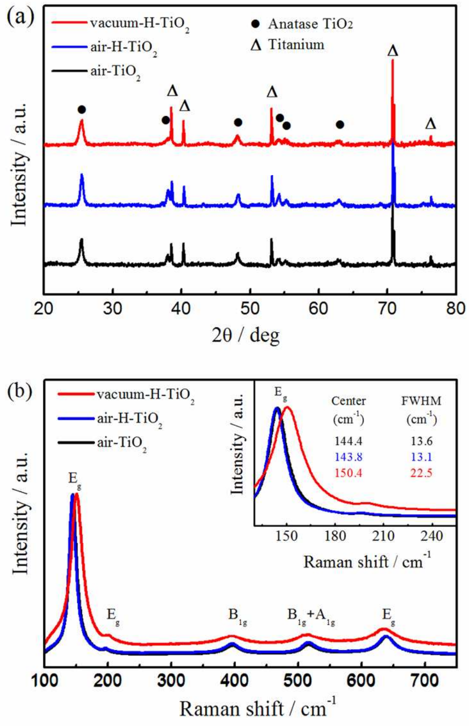

Fig. 7. (a) XRD patterns and (b) Raman spectra of air-TiO_2, air-H-TiO_2, and vacuum-H-TiO_2 samples. Inset in (b) is the enlarged view of Raman spectra for the most intense Eg peak with the corresponding peak positions and widths.

The presence of self-doped Ti^{3+} was examined at room temperature using EPR (Fig. 8). EPR of self-doped Ti^{3+} would give two different peaks for bulk state Ti^{3+} (~1.95) and surface state Ti^{3+} (~2.02).[16] The black vacuum-H-TiO_2 sample gave rise to a very strong EPR signal at 3500 Gauss, while no signal was observed for air-TiO_2 and air-H-TiO_2 samples. This strong EPR signal for a g-value of 1.935 demonstrated the presence of Ti^{3+} in the bulk for vacuum-H-TiO_2 sample. Any surface Ti^{3+} would adsorb atmospheric O_2 and yield a g-value of ~2.02, produced by O_2^- from the reduction of adsorbed O_2. Therefore, the absence of EPR features at a g-value of ~2.02 indicated no Ti^{3+} present on the surface of black vacuum-H-TiO_2 sample.

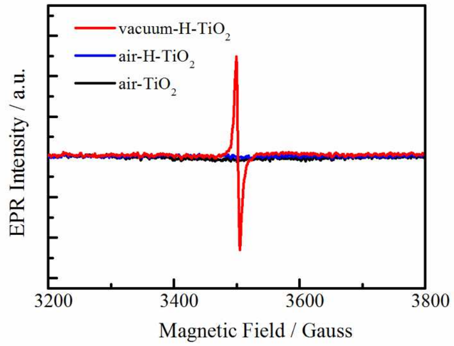

Fig. 8. EPR spectra recorded at room temperature for air-TiO_2, air-H-TiO_2, and vacuum-H-TiO_2 samples.

XPS analysis was employed to further inspect the surface chemical bonding in black hierarchical TiO_2 nanostructures. The Ti $2p_{3/2}$ XPS features were located at 458.61, 458.47, and 458.58 eV for black vacuum-H-TiO_2, air-H-TiO_2, and air-TiO_2 samples, respectively (Fig. 9a). These features were all assigned to Ti^{4+}.[17] If there is Ti^{3+} species existing at the surface, Ti $2p_{3/2}$ feature at 457.37 eV would be expected.[29] This further confirmed that the charge states of Ti atoms at the surface of vacuum-H-TiO_2 sample are Ti^{4+}, and no Ti^{3+} exists at the surface. Similarly, XPS spectra of O 1s region exhibited no obvious difference for air-TiO_2, air-H-TiO_2 and vacuum-H-TiO_2 samples (Fig. 9b). It has been previously reported that the blue-shifts of valence band edge are for black hydrogenated TiO_2.[13, 16] However, the black vacuum-H-TiO_2 nanostructures in this study demonstrated the same valence band maximum as air-TiO_2 and air-H-TiO_2 sample at ~2.65 eV below the Fermi energy (Fig. 9c). Therefore, the surface of black vacuum-H-TiO_2 sample becomes nearly stoichiometric when exposed to air at room temperature after vacuum sintering, which prevents further oxidization of Ti^{3+} in bulk and increases the stability of the black TiO_2; as a result, no shift of the valance band edge occurs.

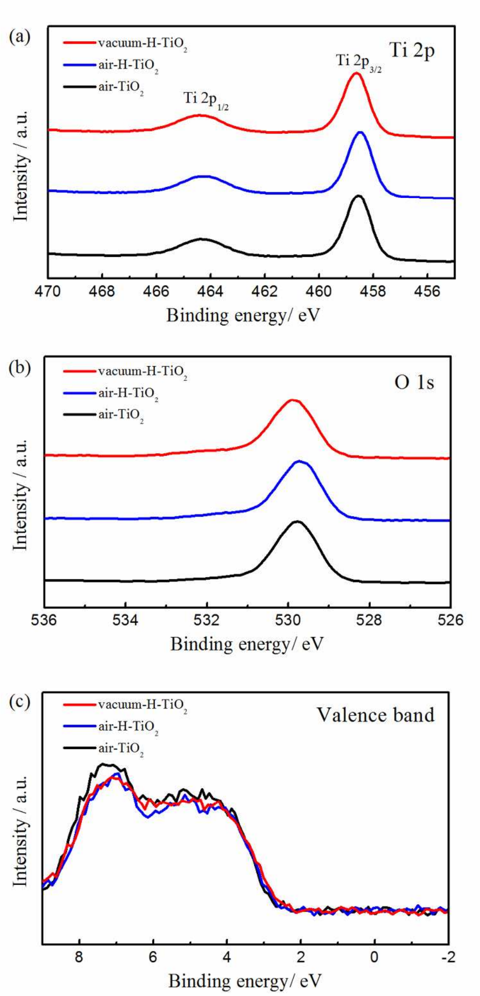

Fig. 9. XPS spectra of (a) Ti 2p, (b) O 1s, and (c) valence band for air-TiO_2, air-H-TiO_2, and vacuum-H-TiO_2 samples.

The doping densities of air-H-TiO_2 and vacuum-H-TiO_2 samples were characterized through the Mott-Schottky plots by EIS measurement. The capacitance (*C*) can be calculated from the imaginary component of the impedance (*Z″*) by $C=1/2\pi f Z''$. Fig. 10 shows the Mott-Schottky plots ($1/C^2$ vs. *E*) achieved for air-TiO_2, air-H-TiO_2 and vacuum-H-TiO_2 samples at 5011 Hz. The doping density (*N*) was inversely proportional to the slope of Mott-Schottky plots:[14, 30]

$$\frac{d(C^{-2})}{dE} = \frac{2}{e\varepsilon\varepsilon_0 N}$$

where *e* is electron charge, ε is dielectric constant of TiO_2 (ε=170), and ε_0 is the vacuum permittivity. The positive slope of Mott-Schottky plots indicated that all samples were *n*-type semiconductors. The calculated donor density based on the slope of Mott-Schottky plots at bias potential from -0.5 V to 0 V was 0.61×10^{20}, 1.42×10^{20} and 1.50×10^{23} cm^{-3} for air-TiO_2, air-H-TiO_2 and vacuum-H-TiO_2 samples, respectively. Even though the Mott-Schottky plots cannot determine the absolute value of donor density, the huge difference indicates an increase in donor density for black vacuum-H-TiO_2 sample compared to the air-TiO_2 and air-H-TiO_2 samples.[14]

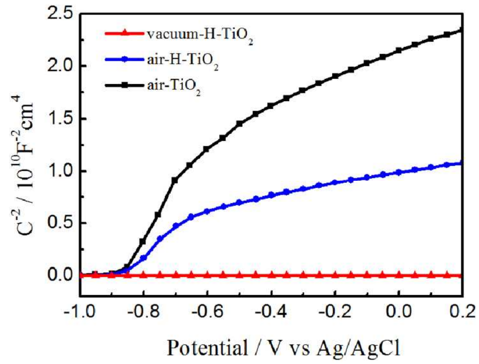

Fig. 10. Mott-Schottky plots of air-TiO_2, air-H-TiO_2, and vacuum-H-TiO_2 samples.

As shown in the UV-vis absorption spectra (Fig. 11), air-H-TiO_2 sample exhibited better absorption in UV light region than air-TiO_2 sample, which was due to the superior light scattering capability of the wire-in-tube morphology. Both the air-H-TiO_2 and air-TiO_2 samples show a similar absorption peak around 400-650 nm, which has been reported before but has unknown origin.[8, 31] Due to the present of this unknown absorption peak at 400-650 nm, it is difficult to analysis the bandgap of these TiO_2 samples by Kubelka-Munk approach. The black vacuum-H-TiO_2 sample showed remarkably increased absorption peaks in the visible light region.

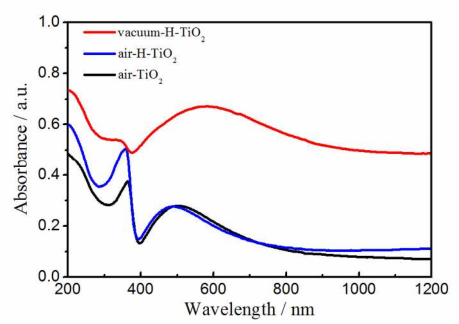

Fig. 11. UV-vis absorbance of air-TiO_2, air-H-TiO_2, and vacuum-H-TiO_2 samples.

The photocatalytic activities of air-TiO_2, air-H-TiO_2, and vacuum-H-TiO_2 samples were investigated by methylene blue (MB) degradation under full spectrum and visible light illumination (Fig. 12). The air-H-TiO_2 samples show improved MB degradation rate than air-TiO_2 samples under full spectrum illumination, while demonstrate almost same photocatalytic activities as air-TiO_2 samples under visible light illumination. This is due to the enhanced UV light absorption and the enlarged surface area for the interaction of MB molecule with photocatalyst for air-H-TiO_2 samples compared to air-TiO_2 samples. The vacuum-H-TiO_2 samples exhibit remarkable MB degradation rate under both full spectrum and visible light illumination. This is ascribed to the reduced bandgap and increased donor density for vacuum-H-TiO_2 samples. During the vacuum annealing, self-doped Ti^{3+} states are introduced into black vacuum-H-TiO_2 sample. This generates localized donor states with an energy level located at 0.75-1.18 eV below the conduction band edge of TiO_2,[32] which reduce the bandgap of black vacuum-H-TiO_2 sample. As a result, the visible light can excite the electron transfer from valence band of black TiO_2 to the oxygen vacancy levels. The visible light induced excitations greatly improve the photocatalytic performance. Moreover, the increased donor density of vacuum-H-TiO_2 samples due to the self-doped with Ti^{3+} can further facilitate the charge transport in TiO_2 photoanode, and leads to efficient photocatalytic activities.

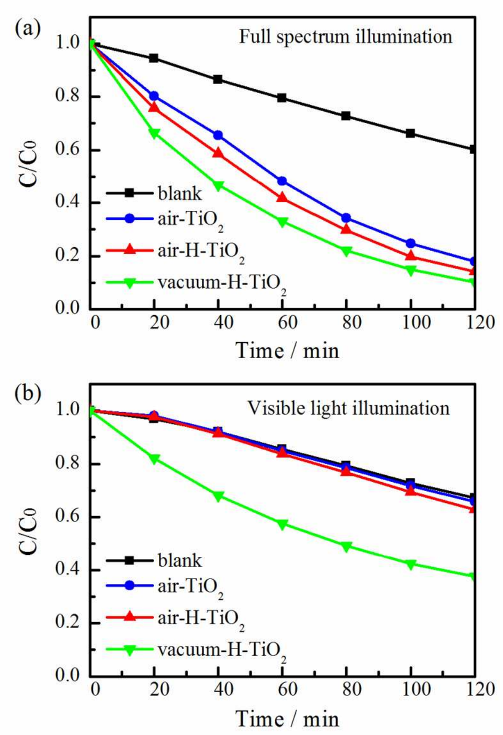

Fig. 12. Photocatalytic activities of air-TiO_2, air-H-TiO_2, and vacuum-H-TiO_2 samples under (a) full spectrum illumination and (b) visible light illumination.

Conclusions

In summary, the hierarchical TiO_2 nanostructures with wire-in-tube architectures were synthesized by a hydrothermal treatment of anodic TiO_2 nanotubes. The morphological evolution was due to the dissolution-precipitation of TiO_6^{2-} octahedra during the hydrothermal treatment. Compared to nanotubular TiO_2, hierarchical TiO_2 nanostructures demonstrate increase photocatalytic activities under UV light range, which is attributed to the increased UV light absorption and the enlarged active interface of photoanode. Moreover, the reduction of TiO_2 architectures by vacuum sintering generated black hierarchical TiO_2 nanostructures. The black hierarchical TiO_2 nanostructures were shown to exhibit an anatase phase with self-doped Ti^{3+} present in the bulk. This resulted from sintering in vacuum conditions which introduced localized donor states below the conduction band edge. Not only did this increase the donor density of black TiO_2 architectures but it also extended the absorption into the visible light region. The photocatalytic activities under full spectrum and visible light illumination of black hierarchical TiO_2 sample were significantly improved compared to the air-sintered samples.

Acknowledgements

The authors acknowledge the financial support from Fundamental Research Program through National Science Foundation and the Institute for Critical Technology and Applied Science of Virginia Tech. The author (S.P.) would also like to acknowledge the support from CERDEC through NSF

I/UCRC CEHMS. Additionally, assistance from Grayson S. Doucette, Andrew Haring, Dr. James Mahaney, Bryce Kidd, Dr. Justin Barone, and Devin Ridgley are greatly appreciated.

Notes and references

[a] Center for Energy Harvesting Materials and Systems, Virginia Tech, 24061 USA. Fax: (540) 231-0745; Tel: (540) 808-3623; E-mail: bochen09@vt.edu, spriya@vt.edu

[b] Department of Chemistry, Virginia Tech, Blacksburg, VA 24061 USA

1. M. Gratzel, *Nature*, 2001, **414**, 338-344.
2. X. B. Chen, S. H. Shen, L. J. Guo and S. S. Mao, *Chem. Rev.*, 2010, **110**, 6503-6570.
3. H. Y. Wang, F. Qian, G. M. Wang, Y. Q. Jiao, Z. He and Y. Li, *ACS Nano*, 2013, **7**, 8728-8735.
4. J. Shi, Y. Hara, C. L. Sun, M. A. Anderson and X. D. Wang, *Nano Lett.*, 2011, **11**, 3413-3419.
5. Y. J. Lin, G. B. Yuan, R. Liu, S. Zhou, S. W. Sheehan and D. W. Wang, *Chem. Phys. Lett.*, 2011, **507**, 209-215.
6. J. Shi and X. D. Wang, *Energy Environ. Sci.*, 2012, **5**, 7918-7922.
7. I. Paramasivam, H. Jha, N. Liu and P. Schmuki, *Small*, 2012, **8**, 3073-3103.
8. Z. H. Zhang and P. Wang, *Energy Environ. Sci.*, 2012, **5**, 6506-6512.
9. C. Das, P. Roy, M. Yang, H. Jha and P. Schmuki, *Nanoscale*, 2011, **3**, 3094-3096.
10. D. A. Wang, Y. Liu, B. Yu, F. Zhou and W. M. Liu, *Chem. Mater.*, 2009, **21**, 1198-1206.
11. Y. C. Wang, Y. Y. Zhang, J. Tang, H. Y. Wu, M. Xu, Z. Peng, X. G. Gong and G. F. Zheng, *ACS Nano*, 2013, **7**, 9375-9383.
12. Z. Y. Liu, Q. Q. Zhang, T. Y. Zhao, J. Zhai and L. Jiang, *J. Mater. Chem.*, 2011, **21**, 10354-10358.
13. X. B. Chen, L. Liu, P. Y. Yu and S. S. Mao, *Science*, 2011, **331**, 746-750.
14. G. Wang, H. Wang, Y. Ling, Y. Tang, X. Yang, R. C. Fitzmorris, C. Wang, J. Z. Zhang and Y. Li, *Nano Lett.*, 2011, **11**, 3026-3033.
15. Z. K. Zheng, B. B. Huang, J. B. Lu, Z. Y. Wang, X. Y. Qin, X. Y. Zhang, Y. Dai and M. H. Whangbo, *Chem. Commun.*, 2012, **48**, 5733-5735.
16. A. Naldoni, M. Allieta, S. Santangelo, M. Marelli, F. Fabbri, S. Cappelli, C. L. Bianchi, R. Psaro and V. Dal Santo, *J. Am. Chem. Soc.*, 2012, **134**, 7600-7603.
17. S. Hoang, S. P. Berglund, N. T. Hahn, A. J. Bard and C. B. Mullins, *J. Am. Chem. Soc.*, 2012, **134**, 3659-3662.
18. X. D. Jiang, Y. P. Zhang, J. Jiang, Y. S. Rong, Y. C. Wang, Y. C. Wu and C. X. Pan, *J. Phys. Chem. C*, 2012, **116**, 22619-22624.
19. S. U. M. Khan, M. Al-Shahry and W. B. Ingler, *Science*, 2002, **297**, 2243-2245.
20. M. G. Walter, E. L. Warren, J. R. McKone, S. W. Boettcher, Q. X. Mi, E. A. Santori and N. S. Lewis, *Chem. Rev.*, 2010, **110**, 6446-6473.
21. I. S. Cho, C. H. Lee, Y. Z. Feng, M. Logar, P. M. Rao, L. L. Cai, D. R. Kim, R. Sinclair and X. L. Zheng, *Nat. Commun.*, 2013, **4**, 1723.
22. Y. Hou, X. Y. Li, Q. D. Zhao, X. Quan and G. H. Chen, *Adv. Funct. Mater.*, 2010, **20**, 2165-2174.
23. B. Chen, J. B. Hou and K. Lu, *Langmuir*, 2013, **29**, 5911-5919.
24. B. Chen, G. S. Doucette and S. Priya, *RSC Advances*, 2013, **3**, 24560-24566.
25. S. P. Albu, A. Ghicov, S. Aldabergenova, P. Drechsel, D. LeClere, G. E. Thompson, J. M. Macak and P. Schmuki, *Adv. Mater.*, 2008, **20**, 4135-4139.
26. M. N. Rahaman, *Ceramic Processing*, CRC Press, Taylor& Francis Group, , 6000 Broken Sound Parkway NW Suite 300, 2007.
27. Q. P. Wu, Q. Zheng and R. van de Krol, *J. Phys. Chem. C*, 2012, **116**, 7219-7226.
28. J. C. Parker and R. W. Siegel, *Appl. Phys. Lett.*, 1990, **57**, 943-945.
29. X. Liu, S. Gao, H. Xu, Z. Lou, W. Wang, B. Huang and Y. Dai, *Nanoscale*, 2013, **5**, 1870-1875.
30. R. Franking, L. S. Li, M. A. Lukowski, F. Meng, Y. Z. Tan, R. J. Hamers and S. Jin, *Energy Environ. Sci.*, 2013, **6**, 500-512.
31. Z. H. Xu and J. G. Yu, *Nanoscale*, 2011, **3**, 3138-3144.
32. X. Y. Pan, M. Q. Yang, X. Z. Fu, N. Zhang and Y. J. Xu, *Nanoscale*, 2013, **5**, 3601-3614.